

# A locally conservative, discontinuous least-squares finite element method for the Stokes equations

Pavel Bochev<sup>1,\*</sup>, James Lai<sup>2</sup> and Luke Olson<sup>2</sup>

<sup>1</sup>*Applied Mathematics and Applications Department, Sandia National Laboratories, Mail Stop 1320, Albuquerque, NM 87185-1320, U.S.A.*

<sup>2</sup>*Department of Computer Science, University of Illinois at Urbana-Champaign, Urbana, IL 61801, U.S.A.*

## SUMMARY

Conventional least-squares finite element methods (LSFEMs) for incompressible flows conserve mass only approximately. For some problems, mass loss levels are large and result in unphysical solutions. In this paper we formulate a new, locally conservative LSFEM for the Stokes equations wherein a discrete velocity field is computed that is point-wise divergence free on each element. The central idea is to allow discontinuous velocity approximations and then to define the velocity field on each element using a local stream-function. The effect of the new LSFEM approach on improved local and global mass conservation is compared with a conventional LSFEM for the Stokes equations employing standard  $C^0$  Lagrangian elements. Copyright © 2011 John Wiley & Sons, Ltd.

Received 1 September 2010; Accepted 6 December 2010

**KEY WORDS:** least-squares finite element methods; discontinuous elements; Stokes equations; locally conservative; stream-function; vorticity; pressure

## 1. INTRODUCTION

A least-squares method for a given partial differential equation (PDE) problem comprises a least-squares functional and a minimization space. The functional is defined by summing the residuals of the PDE measured in suitable Hilbert space norms. If the functional is norm-equivalent on the minimization space, then the resulting unconstrained minimization problem is strongly coercive. Accordingly, conforming discretizations of least-squares principles give rise to well-posed least-squares finite element methods (LSFEMs) for the PDE [1].

LSFEMs have several advantages including naturally satisfying the inf-sup conditions and yielding symmetric and positive-definite linear systems. As a result, in recent years LSFEMs for incompressible flows have grown in popularity; see [1] and the references cited therein for a comprehensive account of the research in this field. Nonetheless, despite their attractive computational and theoretical properties, LSFEMs for incompressible flows have resulted in mixed success and remain in limited use for practical applications. The challenge is that advantageous properties of the LSFEM, such as the reliance on unconstrained residual minimization, also lead to unattractive qualities in the solution. For example, conventional LSFEMs do not fully conserve mass; for some problems, this results in unphysical solutions.

---

\*Correspondence to: Pavel Bochev, Applied Mathematics and Applications Department, Sandia National Laboratories, Mail Stop 1320, Albuquerque, NM 87185-1320, U.S.A.

†E-mail: pbboche@sandia.gov

One of the first attempts to address mass conservation issues in LSFEMs added element-wise mass conservation as an explicit constraint to the least-squares functional and termed the resulting method ‘restricted LSFEM’ [2]. However, this changed the least-squares principle to a saddle-point problem, thereby negating one of the key advantages of LSFEMs over other methods. Subsequently, mass conservation in least-squares methods for the Stokes and the Navier–Stokes equations has been studied extensively in the literature [2–9].

For example, mass conservation in LSFEMs can be improved by modifying the definition of the normal vector at the corner points, or by using least-squares terms to impose weakly the velocity boundary condition [7]. Moreover, a method can be constructed that combines conventional LSFEM with a correction term computed by the so-called  $LL^*$  [10] least-squares approach [7]. Other remedies include alternative formulations of the governing equations obtained by adding new variables and corresponding boundary conditions [5, 6], high order [11] or spectral [8, 9] elements, or weighting the continuity equation more strongly [4]. Compatible finite element spaces are another approach to improved mass conservation. This has been explored in the formulation of a locally conservative *mimetic* LSFEM for the Stokes equations [1, Section 7.7] [12]. However, well-posedness of the mimetic LSFEM has only been established for non-standard boundary conditions specifying the normal velocity and the tangential vorticity on the domain boundary. It is not clear whether or not this method can be extended to the practically important velocity boundary condition.

Consequently, the approaches do not lead to robust solutions to mass conservation. Changing the governing equations requires new boundary conditions which are often difficult to obtain in practical problems. Even more, high-order elements require an increased amount of storage and computation and for this purpose the improvements to mass conservation are not commensurate with the additional cost [5, 7, 9]. More importantly, these approaches, with the exception of the restricted LSFEM [2] and the mimetic LSFEM [12] do not provide *exact* local mass conservation. And, the former leads to a saddle-point problem while the latter requires non-standard boundary conditions.

In this paper we formulate, in two stages, new locally conservative LSFEMs for the Stokes equations with the velocity boundary condition whereby the velocity is approximated by discontinuous finite element spaces that are point-wise divergence free at the interior of each element. We start from a well-posed least-squares formulation for the velocity–vorticity–pressure (VVP) form of the Stokes equations employing conventional  $C^0$  elements. In the first stage we relax the continuity of the velocity space while retaining the other approximating spaces. In this stage we also add least-squares terms to penalize the normal and the tangential jumps of the velocity across the element interfaces. We show that by adjusting the relative importance of the jump terms this intermediate *discontinuous velocity* LSFEM leads to noticeable improvements in the mass conservation. However, the weights required for improved mass conservation differ from problem to problem, thereby making this formulation insufficiently robust for practical applications.

In the second stage, we proceed to define the discontinuous velocity field on each element as the curl of a local stream-function. This guarantees that the velocity is point-wise divergence free on each element. Thus, our approach is viewed as an implementation of the *discontinuous velocity* LSFEM obtained at the first stage, using a locally divergence-free basis for the velocity. We term the resulting method discontinuous stream-function-vorticity–pressure (SVP) LSFEM. Compared to its parent  $C^0$  LSFEM and the intermediate discontinuous velocity LSFEM, the new method offers superior local and global mass conservation.

Our approach is similar to the *discrete* LSFEM [13] for diffusion problems, with two crucial distinctions. First and foremost, the method in [13] is not a discontinuous formulation; in order to handle the discontinuity in the approximating space this method relies on weak discrete differential operators that require inversion of a mass matrix. The second distinction is that in our formulation the velocity field is completely eliminated and we work directly with the stream-function, whereas [13] retains the original fields.

There have been several attempts at discontinuous LSFEMs [14–16]. Discontinuous least-squares formulations are natural extensions of LSFEMs for transmission [17] and mesh-tying problems

[18] from a fixed number of subdomains to an arbitrary number of subdomains. Yet, this idea has not been actively pursued in the context of LSFEMs, likely because of the increased variables in the least-squares first-order system in comparison with Galerkin methods. By using discontinuous elements only for the velocity—the variable that effects mass conservation—our approach, however, reduces the growth of the degrees of freedom relative to a fully discontinuous formulation.

We have organized this paper as follows. The remainder of this section introduces the relevant function space and finite element space notation, and recalls the governing equations. Well-posed prototype *continuous* LSFEMs are reviewed in Section 2. There, we also illustrate the loss of mass in the  $C^0$  least-squares solution. Section 3 is focused on the formulation of the new discontinuous SVP LSFEM, while Appendix A discusses implementation of the LSFEMs in this paper. We demonstrate the usefulness of the new LSFEM through a series of numerical examples presented in Section 4. Conclusions and future work are outlined in Section 5.

### 1.1. Notation

For simplicity we restrict attention to two space dimensions and bounded, simply connected regions  $\Omega \subset \mathbb{R}^2$  with Lipschitz-continuous boundary. In the following we use the standard notation  $H^k(\Omega)$  for the Sobolev space of all square integrable functions that have square integrable derivatives of orders up to  $k$ . The norm and inner product on  $H^k(\Omega)$  are  $\|\cdot\|_k$  and  $(\cdot, \cdot)_k$ , respectively. Further, when  $k=0$  we write  $L^2(\Omega)$ ,  $(\cdot, \cdot)$  and  $\|\cdot\|_0$ . The symbol  $H_0^1(\Omega)$  denotes a subspace of  $H^1(\Omega)$  of functions with vanishing trace on  $\partial\Omega$  and  $L_0^2(\Omega)$  is the subspace of  $L^2$ -fields with vanishing mean. The dual of  $H_0^1(\Omega)$  is the space  $H^{-1}(\Omega)$  with norm

$$\|u\|_{-1} = \sup_{v \in H_0^1(\Omega)} \frac{(u, v)}{\|v\|_1}. \quad (1)$$

Vector-valued fields and their associated function spaces are denoted by bold face symbols. For example,  $\mathbf{u} = (u_1, u_2)$  is a vector-valued field in  $\mathbb{R}^2$  and  $\mathbf{H}^1(\Omega)$  is the Sobolev space of all such fields with components in  $H^1(\Omega)$ . In two dimensions, the curl is defined for scalar and vector functions as

$$\nabla \times \omega = \begin{bmatrix} \omega_y \\ -\omega_x \end{bmatrix} \quad \text{and} \quad \nabla \times \mathbf{u} = (u_2)_x - (u_1)_y, \quad (2)$$

respectively. The symbol  $\mathcal{K}$  stands for a conforming partition of  $\Omega$  into finite elements  $K$ . In two dimensions  $K$  is either a quadrilateral or a triangle, with the interface between two elements denoted by edge  $e$ . The set of all interior edges in the mesh is denoted by  $\mathcal{E}(\Omega)$ , the set of all boundary edges is  $\mathcal{E}(\Gamma)$ , and  $\mathcal{E} = \mathcal{E}(\Omega) \cup \mathcal{E}(\Gamma)$  is the set of all edges in  $\mathcal{K}$ .

The standard  $C^0$  finite element spaces of degree  $r > 0$  on quadrilateral and triangular grids are denoted by  $Q_r$  and  $P_r$ , respectively. We also utilize their discontinuous versions  $[Q_r]$  and  $[P_r]$ . In the following we write  $R_r$  and  $[R_r]$  noting that  $R_r = Q_r$  on quadrilaterals and  $R_r = P_r$  on triangles.

Discontinuous finite element methods require various jump terms on element interfaces. Let  $K_+$  and  $K_-$  be two adjacent elements that share edge  $e$  and let  $\mathbf{u}^+$  and  $\mathbf{u}^-$  denote vector fields defined on each element. Define the jump in normal and tangential components across  $e$  as

$$[\mathbf{u} \cdot \mathbf{n}_e] = \mathbf{u}^+ \cdot \mathbf{n}^+ + \mathbf{u}^- \cdot \mathbf{n}^- \quad \text{and} \quad [\mathbf{u} \times \mathbf{n}_e] = \mathbf{u}^+ \times \mathbf{n}^+ + \mathbf{u}^- \times \mathbf{n}^-, \quad (3)$$

respectively, where  $\mathbf{n}^+$  and  $\mathbf{n}^-$  are the outer normals on  $\partial K^+$  and  $\partial K^-$ , respectively. The jump of a scalar function is defined by the difference

$$[\psi] = \psi^+ - \psi^-. \quad (4)$$

1.2. The governing equations

We recall the primitive variable form of the governing Stokes equations

$$\begin{aligned} -\Delta \mathbf{u} + \nabla p &= \mathbf{f} & \text{in } \Omega \\ \nabla \cdot \mathbf{u} &= 0 & \text{in } \Omega \end{aligned} \tag{5}$$

where  $\mathbf{u}$  and  $p$  are the velocity and the pressure, respectively, and  $\mathbf{f}$  is a given vector function specifying the body force. The system (5) is augmented with the velocity boundary condition

$$\mathbf{u} = \mathbf{0} \quad \text{on } \partial\Omega \tag{6}$$

and the zero mean pressure constraint

$$\int_{\Omega} p \, d\Omega = 0. \tag{7}$$

The first equation in (5) governs conservation of momentum while the second (continuity equation) governs conservation of mass.

To circumvent the need for globally  $H^2$ -conforming finite element spaces, which require  $C^1$  continuity and are difficult to construct, least-squares methods for (5)–(7) are defined using an equivalent first-order form of these equations. There are several first-order formulations of the Stokes equations [1, Section 7.1]. The most widely used is the VVP first-order system

$$\begin{aligned} \nabla \times \omega + \nabla p &= \mathbf{f} & \text{on } \Omega \\ \omega - \nabla \times \mathbf{u} &= 0 & \text{on } \Omega \\ \nabla \cdot \mathbf{u} &= 0 & \text{on } \Omega \end{aligned} \tag{8}$$

which is derived from (5) by using the vorticity  $\omega = \nabla \times \mathbf{u}$  as a new dependent variable and applying the identity  $\nabla \times \nabla \times \mathbf{u} = -\Delta \mathbf{u} + \nabla(\nabla \cdot \mathbf{u})$  to rewrite the momentum equation in terms of the vorticity. The VVP system is augmented with the velocity boundary condition (6) and the zero mean constraint (7).

2. REVIEW OF LEAST-SQUARES FINITE ELEMENT METHODS FOR THE STOKES EQUATIONS

In this section we briefly discuss well-posed LSFEMs for the VVP Stokes equations. We focus on two formulations that employ standard  $C^0$  elements and serve as the basis for our new locally conservative least-squares formulation. The key to a well-posed LSFEM is a norm-equivalent least-squares functional [1]. For the VVP Stokes system, we have the *a priori* bound

$$\|\mathbf{u}\|_1 + \|\omega\|_0 + \|p\|_0 \leq C(\|\nabla \times \omega + \nabla p - \mathbf{f}\|_{-1} + \|\omega - \nabla \times \mathbf{u}\|_0 + \|\nabla \cdot \mathbf{u}\|_0)$$

for any  $\mathbf{u} \in \mathbf{H}_0^1(\Omega) = [H_0^1(\Omega)]^2$ ,  $\omega \in L^2(\Omega)$  and  $p \in L_0^2(\Omega)$ . This bound implies that the *negative norm* functional

$$J_{-1}(\mathbf{u}, \omega, p; \mathbf{f}) = \|\nabla \times \omega + \nabla p - \mathbf{f}\|_{-1}^2 + \|\nabla \times \mathbf{u} - \omega\|_0^2 + \|\nabla \cdot \mathbf{u}\|_0^2 \tag{9}$$

is norm-equivalent on  $X = \mathbf{H}_0^1(\Omega) \times L^2(\Omega) \times L_0^2(\Omega)$ , and that the least-squares principle: *find*  $(\mathbf{u}, \omega, p) \in X$  such that

$$J_{-1}(\mathbf{u}, \omega, p; \mathbf{f}) \leq J_{-1}(\mathbf{v}, \zeta, q; \mathbf{f}) \quad \forall (\mathbf{v}, \zeta, q) \in X \tag{10}$$

is a well-posed unconstrained minimization problem whose minimizer coincides with the solution of the VVP Stokes system. Formally, a well-posed LSFEM is derived by restricting the minimization in (10) to a finite element subspace  $X^h \subset X$ . However, this method is impractical because

$$\|u\|_{-1}^2 = \|(-\Delta)^{-1/2} u\|_0^2.$$

That is, computation of the negative norm requires inversion of the Laplace operator [19]. In order to obtain a practical method the negative norm in (9) must be replaced by a computable discrete approximation. The diagonal operator

$$(-\Delta)^{-1/2} \mapsto h\mathcal{I}, \quad (11)$$

where  $\mathcal{I}$  is the identity, provides a simple, yet sufficiently accurate approximation of the negative norm [1]. Using (11) we obtain a discrete version of (9)

$$J_{-1}^h(\mathbf{u}^h, \omega^h, p^h; \mathbf{f}) = h^2 \|\nabla \times \omega^h + \nabla p^h - \mathbf{f}\|_0^2 + \|\nabla \times \mathbf{u}^h - \omega^h\|_0^2 + \|\nabla \cdot \mathbf{u}^h\|_0^2 \quad (12)$$

and the following discrete least-squares principle: find  $(\mathbf{u}^h, \omega^h, p^h) \in X_r^h$  such that

$$J_{-1}^h(\mathbf{u}^h, \omega^h, p^h; \mathbf{f}) \leq J_{-1}^h(\mathbf{v}^h, \zeta^h, q^h; \mathbf{f}) \quad \forall (\mathbf{v}^h, \zeta^h, q^h) \in X_r^h, \quad (13)$$

where

$$X_r^h = \mathbf{R}_r \cap \mathbf{H}_0^1(\Omega) \times R_{r-1} \times R_{r-1} \cap L_0^2(\Omega), \quad r > 1. \quad (14)$$

We refer to the method (12)–(13) as the *weighted  $L^2$  LSFEM*. This method is a well-posed and optimally convergent<sup>‡</sup> formulation [20]. In particular, the following result holds.

*Theorem 1 (Bochev and Gunzburger [1, Theorem 7.14, p. 262])*

Let  $(\mathbf{u}^h, \omega^h, p^h) \in X_r^h$ ,  $r > 1$  be a solution to (12). Assume that the exact solution of the VVP Stokes system (8) is such that  $\mathbf{u} \in \mathbf{H}^{r+1}(\Omega)$ ,  $\omega \in H^r(\Omega)$  and  $p \in H^r(\Omega)$ . There exists a constant  $C > 0$  such that

$$\begin{aligned} \|\mathbf{u} - \mathbf{u}^h\|_1^2 + \|\omega - \omega^h\|_0 + \|p - p^h\|_0 &\leq Ch^r (\|\mathbf{u}\|_{r+1} + \|\omega\|_r + \|p\|_r) \\ \|\omega - \omega^h\|_1 + \|p - p^h\|_1 &\leq Ch^{r-1} (\|\mathbf{u}\|_{r+1} + \|\omega\|_r + \|p\|_r). \end{aligned} \quad (15)$$

In this paper we restrict attention to implementations of (13) using the *equal-order* space

$$\overline{X}_r^h = \mathbf{R}_r \cap \mathbf{H}_0^1(\Omega) \times R_r(\Omega) \times \check{R}_r(\Omega), \quad r > 1, \quad (16)$$

where  $\check{R}_r$  is the pressure space constrained<sup>§</sup> at a single node on the boundary.

A more robust least-squares method is obtained by using the operator

$$(-\Delta)^{-1/2} \mapsto h\mathcal{I} + (\mathcal{L}^h)^{1/2}, \quad (17)$$

where  $\mathcal{L}^h$  is a spectrally equivalent preconditioner for the Laplace operator [19]. This operator results in a *discrete negative norm*

$$\|\phi^h\|_{-h}^2 = h^2 \|\phi^h\|_0^2 + \|(\mathcal{L}^h)^{1/2} \phi^h\|_0^2 \quad (18)$$

which, for finite element functions, is equivalent to the negative norm (1). Using (18) we obtain a discrete negative norm version of (9)

$$J_{-h}(\mathbf{u}^h, \omega^h, p^h; \mathbf{f}) = \|\nabla \times \omega^h + \nabla p^h - \mathbf{f}\|_{-h}^2 + \|\nabla \times \mathbf{u}^h - \omega^h\|_0^2 + \|\nabla \cdot \mathbf{u}^h\|_0^2 \quad (19)$$

and a well-posed least-squares formulation, which we term the *discrete negative norm LSFEM*. The latter can be discretized using the equal-order space (16) with  $r = 1$  [22]. The error estimates in Theorem 1 continue to hold for the new method, including the case when  $r = 1$  in (16).

<sup>‡</sup>The *minimal approximation condition*  $r > 1$  is required for optimal convergence rates. The violation by using, e.g.  $R_1$  elements for all variables in (14), reduces the accuracy of the least-squares solution; see [20, 21].

<sup>§</sup>For simplicity, we use this approach instead of enforcing (7). The two approaches to elimination of the one-dimensional null-space in the discrete system are equivalent; however, the choice affects the convergence of the iterative method used to solve the system. A comparison and implementation details can be found in [1, Section 7.6.4].

The least-squares functionals (12) and (19) differ only by their treatment of the momentum equation. The use of the discrete negative norm (18) to measure the residual leads to improved conditioning [19] in linear systems, resulting in more efficient solution by preconditioned conjugate gradients. However, compared with the weighted  $L^2$  LSFEM, implementation of the discrete negative norm LSFEM is more involved [22].

Because our strategy for improved mass conservation does not depend on the treatment of the momentum equation, its application to both the weighted  $L^2$  and the discrete negative norm LSFEMs follows a similar process. Therefore, for simplicity and in order to focus on the issue of mass conservation, we use the simpler setting of (12) to motivate the approach and discuss the implementation of the resulting, locally conservative LSFEMs.

### 2.1. Mass conservation in the weighted $L^2$ least-squares method

In this section we present several examples that illustrate the poor mass conservation in conventional LSFEMs. As mentioned, we restrict attention to the weighted  $L^2$  LSFEM; the situation with (19) for these examples follows similarly.

Theorem 1 asserts that both (12) and (19) are optimally accurate for all sufficiently smooth exact solutions of the Stokes equations. This implies that asymptotically  $\|\nabla \cdot \mathbf{u}\| \rightarrow 0$ , as  $h \rightarrow 0$ . However, on a given fixed mesh size this term is not necessarily small and convergence is not guaranteed for solutions with reduced smoothness. The examples in the following support these concerns and highlight that (12) experiences significant mass loss in certain settings.

To this end we consider two standard test problems: the backward-facing step flow, shown in Figure 1, and a channel flow past a cylinder, shown in Figure 2. For the backward-facing step the domain is the rectangle  $[0, 10] \times [0, 1]$  with a re-entrant corner at  $(2, 0.5)$ . The velocity boundary condition is specified as follows. On the inflow ( $x = 0$ ) and outflow ( $x = 10$ ) walls

$$\mathbf{u}_{in} = \begin{bmatrix} 8(y - 0.5)(1 - y) \\ 0 \end{bmatrix} \quad \text{and} \quad \mathbf{u}_{out} = \begin{bmatrix} y(1 - y) \\ 0 \end{bmatrix}, \quad (20)$$

respectively. Along all other parts of the boundary  $\mathbf{u}_{wall} = \mathbf{0}$  is enforced. For this domain, we use a mesh of 900 rectangular elements.

The geometry of the second test problem is given by the rectangle  $[-1, 3] \times [-1, 1]$  with a disk of radius  $r > 0$  centered at  $(0, 0)$ , removed from the domain. We consider two cases:  $r = 0.6$  and

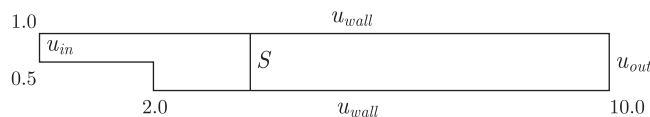


Figure 1. Geometry of the first test problem: backward-facing step.

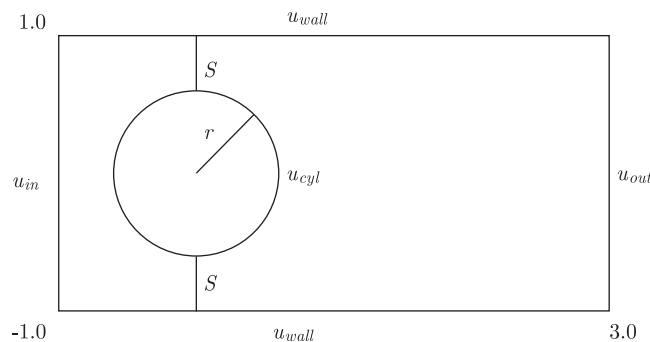


Figure 2. Geometry of the second test problem: flow past a cylinder.

$r=0.9$ . The velocity boundary condition for this problem is set as follows. On the inflow ( $x=-1$ ), outflow ( $x=3$ ), top ( $y=1$ ) and bottom ( $y=-1$ ) walls

$$\mathbf{u}_{\text{in}} = \mathbf{u}_{\text{out}} = \mathbf{u}_{\text{wall}} = \begin{bmatrix} (1-y)(1+y) \\ 0 \end{bmatrix}, \quad (21)$$

and on the surface of the ‘cylinder’  $\mathbf{u}_{\text{cyl}} = \mathbf{0}$ . Therefore, velocity is set to zero on all parts of the boundary except for the inflow and the outflow portions of  $\partial\Omega$ . The mesh for this problem comprises 1296 triangles when  $r=0.6$  and 1104 triangles when  $r=0.9$ .

Specification of the velocity boundary condition in both problems is compatible with  $\nabla \cdot \mathbf{u} = 0$  because fluid enters and leaves the domain only through the inflow and the outflow boundaries, respectively, and

$$\int_{\Gamma_{\text{in}}} \mathbf{u}_{\text{in}} \cdot \mathbf{n} \, d\ell = \int_{\Gamma_{\text{out}}} \mathbf{u}_{\text{out}} \cdot \mathbf{n} \, d\ell.$$

As a result, to assess the mass conservation in the least-squares solution, we measure the total mass flow across a sequence of vertical surfaces connecting the top and the bottom sides of the computational domain. The lines marked by ‘S’ in Figures 1–2 show two typical examples of such surfaces for the two test problems. Because the greatest mass loss for the backward-facing step is expected near the re-entrant corner we always place one of the surfaces at  $x=2$ . For the second test problem we always measure the flow across the surface at  $x=0$  where the domain narrows due to the cylindrical cutout.

In both test problems, velocity is zero on all parts of the boundary except  $\Gamma_{\text{in}}$  and  $\Gamma_{\text{out}}$ . It follows from the divergence theorem that

$$\int_{\Gamma_{\text{in}}} \mathbf{u} \cdot \mathbf{n}_{\text{in}} \, d\ell = \int_S \mathbf{u} \cdot \mathbf{n}_S \, d\ell,$$

for any  $S$  connecting the top and bottom walls of the domain. Therefore, mass conservation is quantified by the percent mass loss across the surface  $S$ , defined as follows:

$$\%m_{\text{loss}} = \frac{\int_{\Gamma_{\text{in}}} \mathbf{u} \cdot \mathbf{n}_{\text{in}} \, d\ell - \int_S \mathbf{u} \cdot \mathbf{n}_S \, d\ell}{\int_{\Gamma_{\text{in}}} \mathbf{u} \cdot \mathbf{n}_{\text{in}} \, d\ell} \times 100. \quad (22)$$

To assess mass conservation properties of the weighted  $L^2$  LSFEM we solve the two test problems using the following modified version of the least-squares functional (12)

$$J_{\mu}^h(\mathbf{u}^h, \omega^h, p^h; \mathbf{f}^h) = h^2 \|\nabla \times \omega^h + \nabla p^h - \mathbf{f}^h\|_0^2 + \|\nabla \times \mathbf{u}^h - \omega^h\|_0^2 + \mu \|\nabla \cdot \mathbf{u}^h\|_0^2 \quad (23)$$

and the equal-order  $C^0$  space (16) with  $r=2$ . This modification was the previously proposed way to improve mass conservation in least-squares methods [4]. By increasing  $\mu$  we increase the relative importance of the residual of the continuity equation, thereby promoting mass conservation. In our study we use  $\mu=1$ ,  $\mu=10$  and  $\mu=20$ .

Our results are summarized in Figure 3. We see that for  $\mu=1$  the least-squares solution of the backward-facing step problem exhibits severe mass loss in excess of 50% of the total mass near the re-entrant corner. Increasing  $\mu$  does improve conservation; however, mass loss remains unacceptably high even for  $\mu=20$ . The mass loss in the second test problem with  $r=0.6$  is less severe but still noticeable at 6%. In this case, setting  $\mu=20$  reduces the loss of mass across the narrowest part of the domain to about 2%. However, as the radius increases to  $r=0.9$ , the mass loss at this location jumps to over 80%. Moreover, setting  $\mu=20$  does not yield noticeable improvement and mass loss remains unacceptably high in excess of 40%. These examples are indicative of the inherent problems with mass conservation in conventional LSFEMs.

We note that significant increase of  $\mu$  is not recommended as it also reduces the accuracy of the other terms in the functional, thus compromising other qualities such as conservation of momentum. Indeed, by increasing the weight of a single term in the least-squares functional, it is

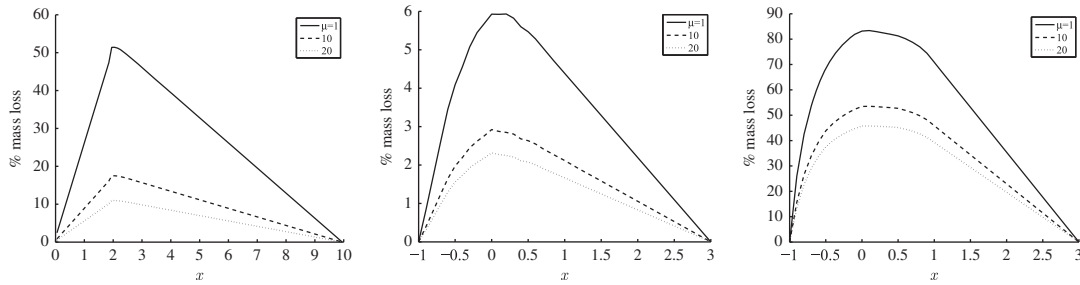


Figure 3. Percent mass loss of (23) for the backward-facing step (left panel) and the flow past a cylinder with  $r=0.6$  (center panel) and  $r=0.9$  (right panel). Values are computed using (22) along vertical lines placed at every 0.1 units along the  $x$ -axis. A total of 100 lines are used for the backward-facing step and 40 lines are used for the flow past a cylinder.

decreasing the importance of the other terms. Thus, by choosing a large weight for  $\mu$  to promote mass conservation, we are effectively demoting conservation of momentum.

*Remark 1*

Exact element-wise mass conservation with  $C^0$  elements has been achieved in the so-called *restricted* least-squares method [2]. In the restricted LSFEM, mass conservation on each element is added as an explicit constraint leading to the following constrained minimization problem:

$$\min_{X_r^h} J_{-1}^h(\mathbf{u}^h, \omega^h, p^h; \mathbf{f}) \quad \text{s.t.} \quad \int_K (\nabla \cdot \mathbf{u}^h) dK = 0 \quad \forall K \in \mathcal{K}. \quad (24)$$

Although (24) returns a solution with exact element-wise mass conservation, this optimization problem is typically solved using Lagrange multipliers and results in a saddle-point system which negates the advantages of using least-squares. The constrained optimization problem can also be solved by a penalty approach, which ultimately leads to a formulation similar to (23) with large  $\mu$ . Because the penalty must be large in order to enforce the constraint accurately, the penalty formulation of (24) suffers from the same disadvantages as (23) with  $\mu \gg 1$ .

In the next section we present an alternative approach to improve mass conservation in least-squares methods based on allowing discontinuous velocity spaces in the formulation.

### 3. DISCONTINUOUS, LOCALLY CONSERVATIVE LEAST-SQUARES FINITE ELEMENT METHOD

Numerical results in the last section show that  $C^0$  LSFEMs suffer from mass loss, exceeding 80% of the total mass for some formulations. Furthermore, the remedies available to counter this loss are not satisfactory: weighting strongly the continuity equation residual as in (23) reduces conservation of momentum, while using the restricted formulation (24) leads to a saddle-point problem.

The option of using div-conforming elements, such as the Raviart–Thomas element [23], to achieve exact mass conservation in least-squares methods has been explored in [12]. However, the resulting mimetic LSFEM requires non-standard boundary conditions for the Stokes equations, and its extension to the practical case of velocity boundary conditions is not clear.

Consequently, in order to improve mass conservation in LSFEMs for the Stokes equations with the velocity boundary condition we propose to employ a *discontinuous* finite element approximation of the velocity, while retaining  $C^0$  elements for the rest of the variables. In so doing we achieve two objectives. First, we keep the growth of the degrees of freedom to a minimum, compared to a fully discontinuous formulation. Second, relaxation of the interelement continuity of the velocity

space allows for a greater flexibility in the choice of the local finite element approximation of that variable. In particular, it becomes possible to consider locally divergence-free spaces which would have been impractical and restrictive if the global velocity space also had to be  $H^1$ -conforming.<sup>‡</sup> Following these ideas we develop locally mass-conservative least-squares formulations based on functionals (12) and (19) in two stages.

### 3.1. Discontinuous velocity least-squares formulation

At the first stage we relax the continuity requirement for the velocity approximating space. Specifically, we change the approximating space from (16) to a space where the first component is discontinuous:

$$\tilde{X}_r^h = [\mathbf{R}_r] \times R_r \times \check{R}_r. \quad (25)$$

To address the loss of conformity in the velocity space we modify (12) and (19). First, the last two terms in these functionals are split into sums over individual elements. Second, we enforce  $H^1$ -conformity weakly by adding residuals of the tangential and normal jumps of the velocity across the element interfaces (edges)  $\mathcal{E}(\Omega)$ ; this methodology is consistent with standard least-squares approaches. As a result, at the first stage we are led to the following *discontinuous velocity* versions of (12) and (19):

$$\begin{aligned} \tilde{J}_{-1}^h(\mathbf{u}^h, \omega^h, p^h; \mathbf{f}^h) &= h^2 \|\nabla \times \omega^h + \nabla p^h - \mathbf{f}^h\|_0^2 + \sum_{K \in \mathcal{K}} (\|\nabla \times \mathbf{u}^h - \omega^h\|_{0,K}^2 + \|\nabla \cdot \mathbf{u}^h\|_{0,K}^2) \\ &+ \sum_{e_i \in \mathcal{E}(\Omega)} h^{-1} (\alpha_1 \|[\mathbf{u} \cdot \mathbf{n}_i]\|_{0,e_i}^2 + \alpha_2 \|[\mathbf{u} \times \mathbf{n}_i]\|_{0,e_i}^2), \end{aligned} \quad (26)$$

$$\begin{aligned} \tilde{J}_{-h}(\mathbf{u}^h, \omega^h, p^h; \mathbf{f}^h) &= \|\nabla \times \omega^h + \nabla p^h - \mathbf{f}^h\|_{-h}^2 + \sum_{K \in \mathcal{K}} (\|\nabla \times \mathbf{u}^h - \omega^h\|_{0,K}^2 + \|\nabla \cdot \mathbf{u}^h\|_{0,K}^2) \\ &+ \sum_{e_i \in \mathcal{E}(\Omega)} h^{-1} (\alpha_1 \|[\mathbf{u} \cdot \mathbf{n}_i]\|_{0,e_i}^2 + \alpha_2 \|[\mathbf{u} \times \mathbf{n}_i]\|_{0,e_i}^2), \end{aligned} \quad (27)$$

where  $\alpha_1, \alpha_2 > 0$  control the relative importance of normal and tangential continuity.

The weights of interface residuals are determined through conditions on the trace. Because the trace of an  $H^1(\Omega)$  function is well-defined in  $H^{1/2}(S)$ , where  $S$  is surface contained in the closure of  $\Omega$ , the proper forms of the interface jump residuals are given by

$$\|[\mathbf{u} \cdot \mathbf{n}_i]\|_{1/2,e_i}^2 \quad \text{and} \quad \|[\mathbf{u} \times \mathbf{n}_i]\|_{1/2,e_i}^2,$$

respectively. However, similar to the negative norm formulation, the trace norm is not easily computable, necessitating a more practical alternative. One straightforward approach is to consider the inverse inequality

$$\|\phi^h\|_{1/2,\partial K}^2 \leq Ch^{-1} \|\phi^h\|_{0,\partial K}^2,$$

which holds for most reasonable finite element partitions and suggests the weighted<sup>‡</sup> trace norms used in (26) and (27). Also, as in the case of the discrete negative norm (18), there are more

<sup>‡</sup>Raviart–Thomas-like elements that are also  $H^1$ -conforming, i.e. continuous across element interfaces, can be constructed on rectangular grids using tensor products of one-dimensional quadratic Lagrange and cubic Hermite shape functions [24]. Using such elements could lead to a least-squares formulation which computes solenoidal velocity fields. However, the scope of such a formulation would be limited to regions that could be meshed entirely by rectangular elements. Our second test problem is one example where this is not feasible.

<sup>‡</sup>We note that identically weighted norms were used in [7] to weakly enforce the velocity boundary condition.

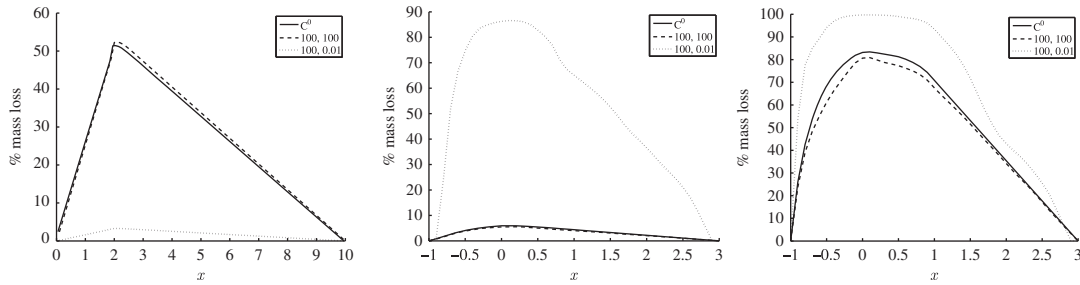


Figure 4. Percent mass loss in the discontinuous velocity least-squares method (26) for the backward-facing step (left panel) and the flow past a cylinder with  $r=0.6$  (center panel) and  $r=0.9$  (right panel). Dashed line corresponds to  $\alpha_1=\alpha_2=100$ , dotted line corresponds to  $\alpha_1=100, \alpha_2=0.01$  and the solid line gives the reference mass loss by the prototype  $C^0$  least-squares method (12). The legend values are read as  $\alpha_1, \alpha_2$  with (12) as reference labeled ( $C_0$ ). Values are computed using (22) along vertical lines placed at every 0.1 units along the  $x$ -axis. A total of 100 lines are used for the backward-facing step and 40 lines are used for the flow past a cylinder.

sophisticated alternatives to weighted trace norms defined by using special boundary functionals [25]. Discussion of such functionals is beyond the scope of this paper.

*Remark 2*

The functionals (26)–(27) obtained at the end of the first stage may also be viewed as extensions of the least-squares formulation for transmission problems [26] to the VVP Stokes system with one important distinction. Namely, the interface coupling terms are applied only to the velocity because the vorticity and the pressure remain approximated by  $C^0$  elements. See [15, 16, 18] for further examples of domain-decomposition and discontinuous least-squares formulations.

*3.1.1. Mass conservation of the discontinuous velocity least-squares formulation.* In view of div-conforming elements, one approach is to improve the mass conservation in the finite element solution of (26) and (27) by strengthening the normal continuity of the velocity field. On the other hand, the discontinuous velocity formulations (26) and (27) with  $\alpha_1 \gg \alpha_2$  directly target reduction in mass loss for our two test problems. To test this hypothesis we implement (26) using the equal-order, discontinuous velocity finite element space (25) with  $r=2$  and solve the two test problems with two different choices for  $\alpha_1$  and  $\alpha_2$ . The first choice is to set  $\alpha_1=\alpha_2=100$ , in which case we expect\*\* to see mass losses comparable to that in the original  $C^0$  formulation (12). The second set of weights  $\alpha_1=100, \alpha_2=0.01$  emphasizes normal over tangential continuity. The expectation is that this set of weights leads to an improved mass conservation. Unfortunately, the results shown in Figure 4 do not support our conjecture that mass loss can be controlled by interelement continuity alone. Indeed, the left panel in the figure shows that for the backward-facing step problem the second weight combination leads to a *significant improvement* in the mass conservation by reducing the mass loss from over 50% to just over 3%. However, the situation is reversed for the second test problem with  $r=0.6$ . Now the choice  $\alpha_1=100, \alpha_2=0.01$  leads to a *significant deterioration* of the mass conservation and increases mass loss from 6% in the  $C^0$  formulation to *nearly 90%* in the discontinuous velocity LSFEM. When the radius increases to  $r=0.9$  the same weight combination leads to a *nearly complete* mass loss, as shown in the right panel of Figure 4.

These results indicate that the discontinuous velocity formulation (26) cannot be reliably counted on to always improve mass conservation with the same choice of weights. Or, more precisely, mass conservation properties are problem dependent. We thus focus on this issue in the second stage of the formulation of our new method.

\*\*This is because in the limit as  $\alpha_1 \rightarrow \infty$  and  $\alpha_2 \rightarrow \infty$ , (26) recovers the  $C^0$  solution of the weighted  $L^2$  LSFEM method.

### 3.2. Discontinuous stream-function least-squares formulation

To motivate this stage we note that while discontinuous velocity functionals (26) and (27) enable some improvements in mass conservation, they do not enforce mass conservation locally on each element. At the same time, considering that the velocity space is not subject to any interelement continuity, with (26) and (27) we have greater flexibility for choosing the velocity representation on each element than with (12) and (19). In particular, we are able to force the velocity to be *point-wise* divergence-free on each element by setting

$$\mathbf{u}^h|_K = \nabla \times \psi^h|_K \quad \forall K \in \mathcal{K}, \quad (28)$$

where  $\psi^h \in [R_{r+1}]$  is a discontinuous *stream-function*. The finite element space for  $\psi^h$  is of one degree higher than the original velocity finite element space to ensure that  $\nabla \times \psi^h \in [\mathbf{R}_r]$ .

Thus, at the second stage we replace the velocity approximation in (26) and (27) with the field defined in (28). Note that in this definition of  $\mathbf{u}^h$ , we have that  $\nabla \cdot \mathbf{u}^h = 0$  is automatically satisfied. In response, we drop the residual of the continuity equation from the least-squares functional and add a term that penalizes the jump of the stream-function. Furthermore, because velocity is eliminated, the velocity boundary condition is imposed through the stream-function. Since  $\mathbf{n} \cdot \nabla \times \psi^h$  involves only tangential derivatives of  $\psi^h$ , a Dirichlet boundary condition on the stream-function prescribes the normal component of the velocity. We specify the tangential component of the velocity weakly by adding its residual to the least-squares functional. In summary, at the end of the second stage, the discontinuous velocity functionals (26) and (27) are transformed into the following *discontinuous stream-function-vorticity-pressure* functionals:

$$\begin{aligned} \tilde{J}_{-1}^h(\psi^h, \omega^h, p^h; \mathbf{f}^h) &= h^2 \|\nabla \times \omega^h + \nabla p^h - \mathbf{f}^h\|_0^2 + \sum_{K \in \mathcal{K}} \|\nabla \times \nabla \times \psi^h - \omega^h\|_{0,K}^2 \\ &+ \sum_{e_i \in \mathcal{E}(\Omega)} h^{-1} (\|[(\nabla \times \psi^h) \cdot \mathbf{n}_i]\|_{0,e_i}^2 + \|[(\nabla \times \psi^h) \times \mathbf{n}_i]\|_{0,e_i}^2) \\ &+ \sum_{e_i \in \mathcal{E}(\Gamma)} h^{-1} \|(\nabla \times \psi^h) \times \mathbf{n}_i\|_{0,e_i}^2 + \sum_{e_i \in \mathcal{E}(\Omega)} h^{-3} \|[\psi^h]\|_{e_i}^2, \end{aligned} \quad (29)$$

$$\begin{aligned} \tilde{J}_{-h}^h(\psi^h, \omega^h, p^h; \mathbf{f}^h) &= \|\nabla \times \omega^h + \nabla p^h - \mathbf{f}^h\|_{-h}^2 + \sum_{K \in \mathcal{K}} \|\nabla \times \nabla \times \psi^h - \omega^h\|_{0,K}^2 \\ &+ \sum_{e_i \in \mathcal{E}(\Omega)} h^{-1} (\|[(\nabla \times \psi^h) \cdot \mathbf{n}_i]\|_{0,e_i}^2 + \|[(\nabla \times \psi^h) \times \mathbf{n}_i]\|_{0,e_i}^2) \\ &+ \sum_{e_i \in \mathcal{E}(\Gamma)} h^{-1} \|(\nabla \times \psi^h) \times \mathbf{n}_i\|_{0,e_i}^2 + \sum_{e_i \in \mathcal{E}(\Omega)} h^{-3} \|[\psi^h]\|_{e_i}^2. \end{aligned} \quad (30)$$

The weight for last term in (29) and (30) is determined by an inverse inequality, analogous to that of the velocity jump terms, but assuming that  $\psi \in H^2(\Omega)$  and hence its trace is in  $H^{3/2}(S)$  where  $\Omega$  and  $S$  are as defined previously for the discontinuous velocity formulation. The jump of the stream-function is necessary for elements not adjacent to the boundary as constraining only  $[\mathbf{n} \cdot \nabla \times \psi^h]$  and  $[\mathbf{n} \times \nabla \times \psi^h]$  specifies  $\psi^h$  only up to a constant.

We associate with (29) the least-squares principle: *find*  $(\Psi^h, \omega^h, p^h) \in \tilde{W}_r^h$  *such that*

$$\tilde{J}_{-1}^h(\Psi^h, \omega^h, p^h; \mathbf{f}) \leq \tilde{J}_{-1}^h(\Phi^h, \zeta^h, q^h; \mathbf{f}) \quad \forall (\Phi^h, \zeta^h, q^h) \in \tilde{W}_r^h, \quad r > 1 \quad (31)$$

where the approximating space is given by

$$\tilde{W}_r^h = [R_{r+1}] \times R_r \times \check{R}_r. \quad (32)$$

The least-squares principle for (30) is similar except that we allow for  $r = 1$  in the definition of the finite element space (32). Once (31) or its discrete negative norm companion are solved, the velocity is recovered using (28): on each element  $\mathbf{u}^h|_K = \nabla \times \psi^h|_K$ .

*Remark 3*

An alternative approach to the derivation of our discontinuous SVP least-squares method is to start directly with a stream-function vorticity formulation of the governing equations. For examples of various numerical methods based on this approach we refer to [27–29] and solution methods for the resulting equations are discussed in [30, 31]. Our approach is advantageous for two reasons. First, it clearly shows the connection with some of the most popular least-squares formulations for the Stokes equations. More importantly, our approach exposes the resulting discontinuous SVP formulations as special cases of the discontinuous velocity LSFEMs with a specific choice of a *divergence-free* basis. In this paper we choose to define this basis through a stream-function as in (28) primarily because of the simplicity of this choice; however, it should be clear that our approach can easily accommodate any choice of a divergence-free velocity basis. For examples of discontinuous Galerkin methods that adhere to the latter strategy we refer to [32, 33], and the references therein.

*Remark 4*

It is worth pointing out that the flux in the discrete least-squares method for the Darcy flow in two dimensions [13] is approximated by a similar discontinuous space  $\mathbf{V}^h = \nabla(V_D^h) \oplus \nabla \times (V_N^h)$  where  $V_D^h$  and  $V_N^h$  are standard  $C^0$  finite element spaces constrained by zero on the Dirichlet and Neumann portions of the boundary. The key difference is that our approach deals with the discontinuity of the approximating space by including appropriate jump terms and retaining the original differential operators, whereas [13] retains the global inner products and switches to weak discrete differential operators defined using integration by parts.

## 4. NUMERICAL EXAMPLES

The main objective of this section is to demonstrate the attractive computational properties of the new discontinuous SVP least-squares formulation (29). We utilize a manufactured solution to estimate the convergence rates of the new method and then examine its mass conservation properties using the test problems defined in Section 2.1.

We use the Trilinos [34] package Intrepid [35] to implement the SVP formulation (29), as described in Appendix A, on triangular and quadrilateral grids. The finite element space is (32) with  $r=2$ , that is,

$$\tilde{W}_2^h = [R_3] \times R_2 \times \check{R}_2.$$

The approximation of the stream-function by  $[R_3]$  elements is consistent with the requirement<sup>††</sup> that the velocity in the parent least-squares formulation (12) should be approximated by at least  $\mathbf{R}_2$  elements. Violation of this requirement has negative consequences for the accuracy of (12) [20]. To assess the relevance of this requirement for the SVP formulation, in Section 4.2 we include comparisons with an implementation of the new method which uses the equal-order space

$$\widehat{W}_2^h = [R_2] \times R_2 \times \check{R}_2.$$

## 4.1. Rates of convergence

This study uses a sequence of five uniform partitions of the unit square  $[0, 1] \times [0, 1]$  into square elements with side lengths of  $h_i = 2^{-i}$ ,  $i = 1, 2, 3, 4, 5$ . Suppose that  $e_i$  is the error corresponding to mesh size  $h_i$ . We use incremental linear regression to generate a sequence of convergence rate estimates  $\alpha_i$ ,  $i = 2, 3, 4, 5$ . Specifically,  $\alpha_i$  is the slope of the best least-squares fit to the data points  $\{(-k, \log_2 e_k)\}_{k=1, i}$ .

<sup>††</sup>We note that this minimal approximation condition does not extend to the negative norm LSFEM (19).

To generate the error data  $e_i$  we solve the SVP formulation (29) with a right-hand side and boundary data corresponding to the exact solution

$$\psi = \cos(\pi x) + \cos(\pi y), \quad \omega = \nabla \times \nabla \times \psi = \pi^2(\cos(\pi x) + \cos(\pi y)), \quad p = \cos(x)\exp(y),$$

which leads to

$$\mathbf{f} = \begin{bmatrix} -\pi^3 \sin(\pi y) - \exp(y) \sin(x) \\ \pi^3 \sin(\pi x) + \exp(y) \cos(x) \end{bmatrix}.$$

Because the discontinuous SVP formulation is derived from the weighted  $L^2$  LSFEM (12), and the minimal approximation condition is satisfied, we anticipate convergence rates for the vorticity and the pressure to be at least as predicted by Theorem 1 for  $r=2$ . However, our implementation uses vorticity and pressure spaces of one degree higher than in the statement of the theorem. As a result, it is reasonable to expect that

$$\|p - p^h\|_0 = \|\omega - \omega^h\|_0 = O(h^3) \quad \text{and} \quad \|p - p^h\|_1 = \|\omega - \omega^h\|_1 = O(h^2).$$

The rates of convergence for the stream-function cannot be inferred directly from the theorem. Nonetheless, knowing that the SVP formulation originates in the optimally accurate and well-posed LSFEM (12), we anticipate that convergence rates for this variable will be close to the best approximation theoretic rates for  $R_3$  elements.

These conjectures are largely confirmed by the data in Tables I–III, except for the  $L^2$  rate of the stream-function which is less than the expected value of 4. However, as the mesh is refined, the  $H^1$ -seminorm error rate for this variable approaches the best theoretical value of 3. As a rule,  $L^2$  rates tend to be less reliable and so further theoretical studies are necessary to establish the convergence of the new SVP formulation. Nevertheless, the preliminary convergence results reported here are encouraging and suggest that the SVP formulation is optimally accurate.

#### 4.2. Conservation of mass

In this section we demonstrate improved mass conservation in the SVP formulation (29) through several computational examples. We use the backward-facing step and the flow past a cylinder

Table I. Error and convergence rate estimates for the stream-function.

$h$	$\ \psi - \psi^h\ _0$	Rate	$\ \psi - \psi^h\ _1$	Rate
$\frac{1}{2}$	4.555e-03		5.431e-02	
$\frac{1}{4}$	4.014e-04	3.50	6.886e-03	2.98
$\frac{1}{8}$	3.767e-05	3.46	1.004e-03	2.88
$\frac{1}{16}$	5.280e-06	3.27	1.340e-04	2.88
$\frac{1}{32}$	6.976e-07	3.16	1.711e-05	2.89

Table II. Error and convergence rate estimates for the vorticity.

$h$	$\ \omega - \omega^h\ _0$	Rate	$\ \omega - \omega^h\ _1$	Rate
$\frac{1}{2}$	1.216e+00		1.072e+01	
$\frac{1}{4}$	1.079e-01	3.49	1.600e+00	2.74
$\frac{1}{8}$	1.200e-02	3.33	3.257e-01	2.52
$\frac{1}{16}$	1.486e-03	3.22	8.037e-02	2.35
$\frac{1}{32}$	1.938e-04	3.14	2.258e-02	2.21

Table III. Error and convergence rate estimates for the pressure.

$h$	$\ p - p^h\ _0$	Rate	$\ p - p^h\ _1$	Rate
$\frac{1}{2}$	1.895e+00		1.054e+01	
$\frac{1}{4}$	1.750e-01	3.44	1.446e+00	2.87
$\frac{1}{8}$	1.676e-02	3.41	2.688e-01	2.65
$\frac{1}{16}$	1.913e-03	3.32	6.188e-02	2.47
$\frac{1}{32}$	2.529e-04	3.23	1.515e-02	2.34

test problems shown in Figures 1 and 2, respectively. First, we compare and contrast the mass loss in (12) and (29) using the same grids as in Section 2.1: 900 rectangular elements for the backward-facing step; 1296 triangular elements for the flow past a cylinder with  $r = 0.6$  and 1104 triangular elements for  $r = 0.9$ . We also investigate the relevance of the minimal approximation condition for the mass conservation in the SVP formulation by comparing the mass losses in implementations of (29) with  $[R_3]$  and  $[R_2]$  elements for the stream-function, respectively. Our final study examines improvement in the mass conservation under mesh refinement.

Recall that in the SVP formulation the normal component of the velocity boundary condition is prescribed through an equivalent Dirichlet condition on the stream-function, and that the tangential component is enforced weakly by including its residual in (29). In the case of the backward-facing step, the velocity boundary condition is given by (20). On  $\Gamma_{\text{in}}$  and  $\Gamma_{\text{out}}$  velocity is only a function of  $y$  and  $\mathbf{u} \cdot \mathbf{n} = \pm u_1$ . Integration of  $u_1$  along  $\Gamma_{\text{in}}$  and  $\Gamma_{\text{out}}$  yields an equivalent Dirichlet boundary condition on the stream-function:

$$\psi_{\text{in}} = -\frac{8}{3}y^3 + 6y^2 - 4y + C_1 \quad \text{and} \quad \psi_{\text{out}} = \frac{y^2}{2} - \frac{y^3}{3} + C_2.$$

The constants  $C_1$  and  $C_2$  are chosen so that  $\mathbf{u}_{\text{in}}(0.5) = \mathbf{u}_{\text{out}}(0)$  and  $\mathbf{u}_{\text{in}}(1) = \mathbf{u}_{\text{out}}(1)$ . On the top and the bottom walls  $\psi$  is set to a constant value equal to  $\mathbf{u}_{\text{in}}(1)$  and  $\mathbf{u}_{\text{in}}(0.5)$ , respectively.

For the flow past a cylinder the velocity boundary condition is specified in (21). An equivalent Dirichlet condition on the stream-function, which prescribes the same normal velocity component is given by

$$\psi_{\text{in}} = \psi_{\text{out}} = \psi_{\text{wall}} = y - \frac{y^3}{3}.$$

Because  $\mathbf{u} \times \mathbf{n} = 0$  on  $\partial\Omega$  for both test problems, accounting for this part of the velocity boundary condition does not require additional terms beyond adding its residual, written as  $(\nabla \times \psi) \times \mathbf{n}$ , to the least-squares functional (29).

Results from our first study are summarized in Figure 5. The mass losses in the new SVP formulation (29) are compared to its parent LSFEM (12) for the backward-facing step and for the flow past a cylinder with  $r = 0.6$  and  $r = 0.9$ . In all three cases the SVP solution shows significant improvements in the mass conservation, as measured by the percent mass loss formula (22). For the backward-facing step, the maximum mass loss is less than 0.5% with most of the mass loss localized at the re-entrant corner. On the rest of the domain, the solution is basically conserved over any closed subdomain. For the flow past a cylinder, the center and right panels in Figure 5 reveal that the mass loss in the new SVP formulation does not deteriorate as the radius of the cylinder increases from 0.6 to 0.9. In the narrowest region of the computational domain the global mass in the SVP solution fluctuates within less than 1%, and in the rest of the domain it is essentially constant. These results clearly show that mass conservation in the new SVP formulation is superior to that of the weighted  $L^2$  (12) and the discontinuous velocity LSFEM (26).

Figure 6 shows the results of our second study, which compares conservation properties of (29) implemented with  $[R_3]$  and  $[R_2]$  elements for the stream-function, respectively. The objective is

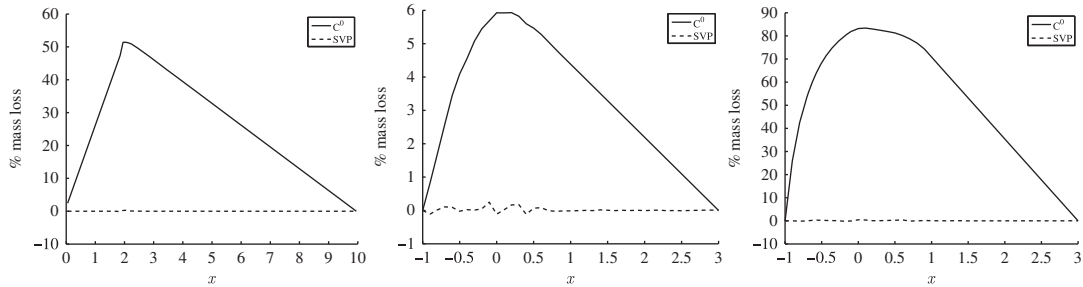


Figure 5. Comparison of mass loss in (12) and (29) for the backward-facing step (left panel) and the flow past a cylinder with  $r=0.6$  (center panel) and  $r=0.9$  (right panel). Solid line represents the weighted  $L^2$  formulation (12), dashed line is the new SVP formulation (29). Values are computed using (22) along vertical lines placed at every 0.1 units along the  $x$ -axis. A total of 100 lines are used for the backward-facing step and 40 lines are used for the flow past a cylinder.

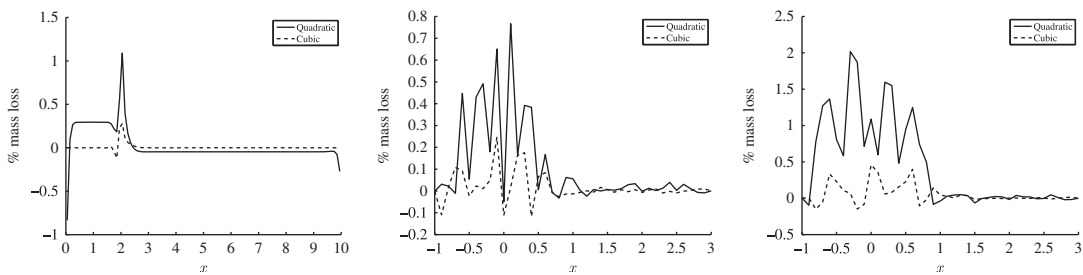


Figure 6. Comparison of mass loss in (29) implemented with  $[R_2]$  and  $[R_3]$  elements for the stream-function, for the backward-facing step (left panel) and the flow past a cylinder with  $r=0.6$  (center panel) and  $r=0.9$  (right panel). Solid line represents implementation of (29) with an  $[R_2]$  stream-function, dashed line corresponds to an  $[R_3]$  stream-function. Values are computed using (22) along vertical lines placed at every 0.1 units along the  $x$ -axis. A total of 100 lines are used for the backward-facing step and 40 lines are used for the flow past a cylinder.

to determine whether the SVP formulation inherits the minimal approximation condition from its parent LSFEM (12) as a strong, dominant trait. If this were the case, then an SVP implementation employing the equal-order space  $\widehat{W}_2^h = [R_2] \times R_2 \times \widehat{R}_2$  should experience noticeable deterioration in the mass conservation. However, the plots in Figure 6 suggest that this is not the case, and that the SVP formulation continues to exhibit high performance with an  $[R_2]$  stream-function. For the backward-facing step, the switch from  $[R_3]$  to  $[R_2]$  elements causes the maximum mass loss to grow from 0.5 to 1.09%. For the flow past a cylinder with  $r=0.6$ , the maximum loss grows from 0.3 to 0.8%, and for  $r=0.9$  we see the greatest growth from 0.4 to 2%. However, even with these increases, the mass loss in all three test problems remains within acceptable limits and well below the mass losses in (12) and (26). Based on these results we conclude that the minimal approximation condition is not a principal limitation for the SVP formulation as it is for its  $C^0$  parent (12). The possibility to implement (29) with equal-order elements without serious deterioration in accuracy is valuable from an efficiency standpoint because such elements have more uniform data structures.

Our third study examines improvement in mass conservation under refinement. For this study the original finite element partitions for the backward-facing step and for the flow past a cylinder problems were uniformly refined to grids with four times as many elements. Thus, the refined grids comprise 3600 rectangular elements for the backward-facing step, 5184 triangle elements for the flow past a cylinder of radius 0.6 and 4416 triangle elements for the flow past a cylinder with radius 0.9. Results of the refinement study are shown in Figure 7. The most significant improvement occurs in the backward-facing step problem where the maximum mass loss decreases almost five-fold from 0.28 to 0.06%. We see the same improvement in the flow past a cylinder of

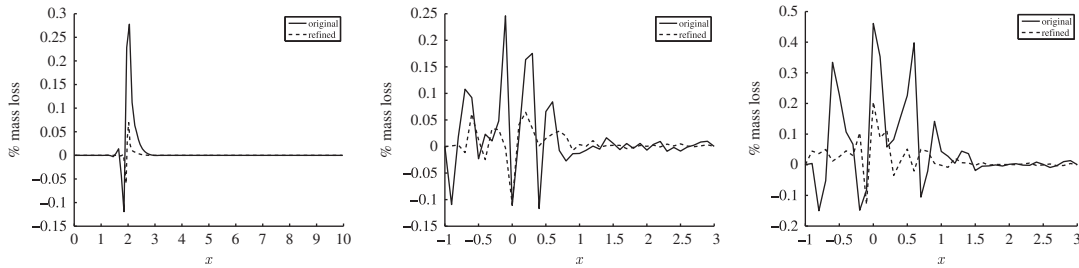


Figure 7. Improvement of the mass conservation in (29) under mesh refinement for the backward-facing step (left panel) and the flow past a cylinder with  $r=0.6$  (center panel) and  $r=0.9$  (right panel). The solid and the dashed line represent the SVP formulation (29) on the original and on the refined meshes, respectively. Values are computed using (22) along vertical lines placed at every 0.1 units along the  $x$ -axis. A total of 100 lines are used for the backward-facing step and 40 lines are used for the flow past a cylinder.

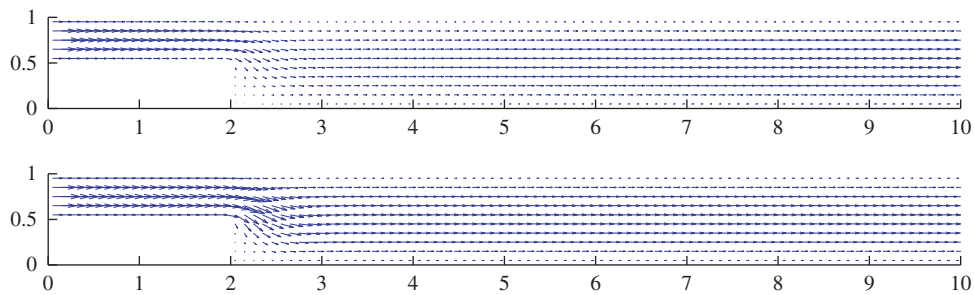


Figure 8. Velocity plot of the weighted  $L^2$  LSFEM (12) (top) and the SVP formulation (29) (bottom) for the backward-facing step.

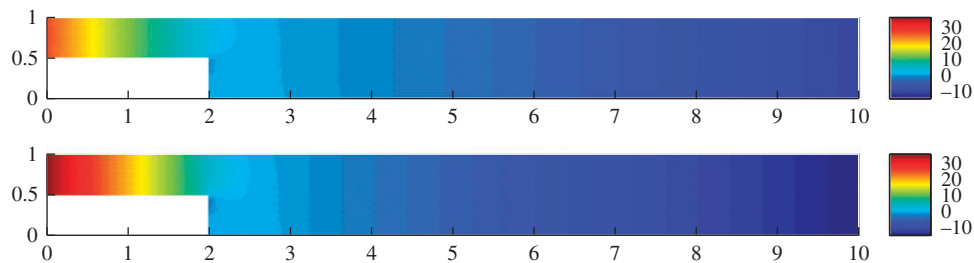


Figure 9. Pressure plot of the weighted  $L^2$  LSFEM (12) (top) and the SVP formulation (29) (bottom) for the backward-facing step.

radius 0.6. The reduction in the maximum mass loss when  $r=0.9$  is somewhat smaller, but still valuable. The important conclusion from this study is that mesh refinement consistently delivers further improvements to the mass conservation of the SVP formulation.

Additionally, there are some qualitative differences in the finite element solutions computed by (29) and (12), which can be attributed to the mass losses in the latter. Plots of the velocity, pressure and vorticity for the backward-facing step problem computed by these two methods are compared in Figures 8–10. One significant difference between the two solutions is seen in the velocity plots shown in Figure 8. The SVP solution exhibits the expected behavior near the re-entrant step and maintains the characteristic parabolic velocity profile throughout the full length of the problem domain. In contrast, the severe mass loss in the solution of (12) near the re-entrant step leads to an underestimate of the velocity magnitude and weakening of its parabolic profile in this region.

Plots of the finite element solutions for (29) and (12) in the case the flow past a cylinder of radius 0.6 are compared in Figures 11–13. The computed velocity fields by (29) and (12) are

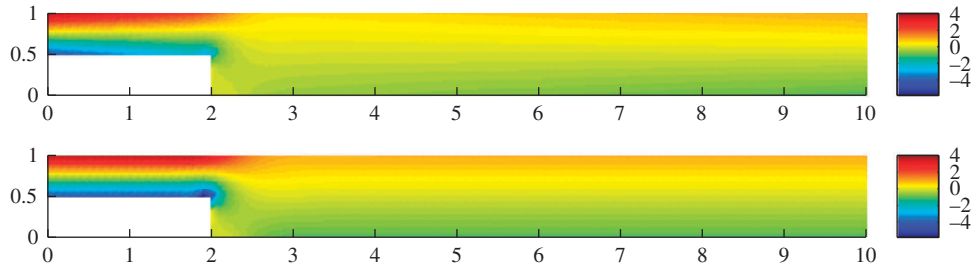


Figure 10. Vorticity plot the weighted  $L^2$  LSFEM (12) (top) and the SVP formulation (29) (bottom) for the backward-facing step.

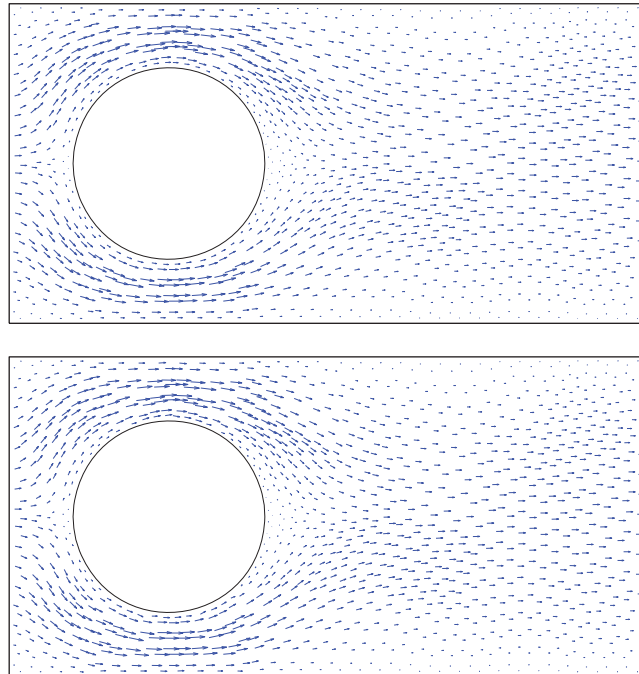


Figure 11. Velocity plot of the weighted  $L^2$  LSFEM (12) (top) and the SVP formulation (29) (bottom) for the flow past a cylinder with  $r=0.6$ .

similar for this example since the maximum mass loss in the case of (12) is only 6%. However, even for this case of low mass loss, the inadequate pressure drop in the region behind the cylinder is noticeable, as depicted in Figure 12. Visible differences are also evident in the vorticity plots shown in Figure 13.

However, setting the cylinder radius to 0.9 intensifies the difficulty for (12), which now exhibits a loss of over 80% of the mass in the narrowest region—see Figure 3. Accordingly, the qualitative differences between the solutions of (29) and (12) become more pronounced, especially for the velocity and the pressure. Because the cylinder restricts 90% of the channel, the fluid velocity must increase significantly in the regions between the boundary walls and the top and the bottom of the cylinder. As shown in Figure 14, the SVP solution demonstrates this behavior. In contrast, the magnitude of the velocity in the solution of (12) is comparable to that of the inflow boundary, thus underestimating the velocity. In Figure 15 we also observe that the pressure drop behind the cylinder in the solution to (12) is underestimated. Moreover, as before, the visible qualitative differences extend to the vorticity plots in Figure 16.

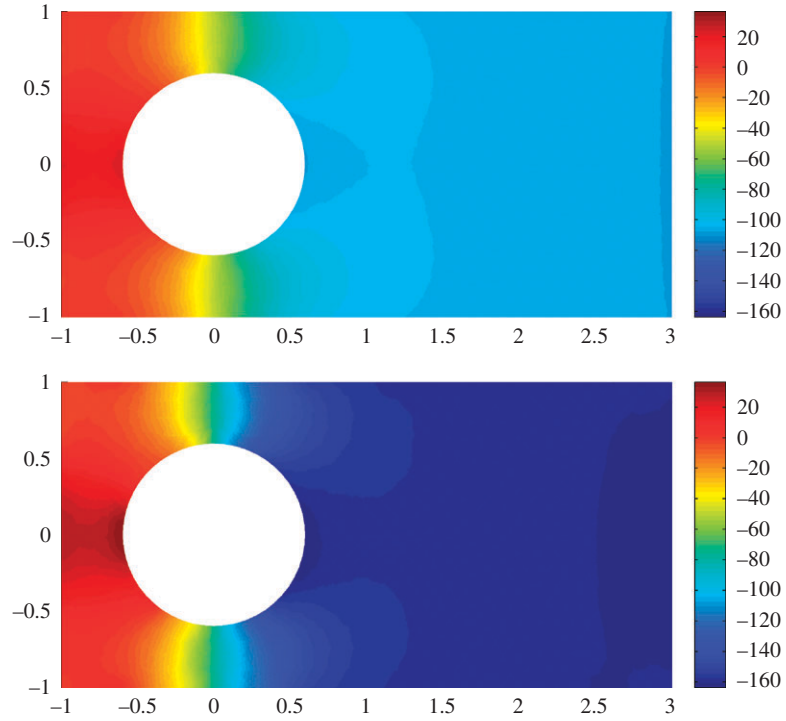


Figure 12. Pressure plot of the weighted  $L^2$  LSFEM (12) (top) and the SVP formulation (29) (bottom) for the flow past a cylinder  $r=0.6$ .

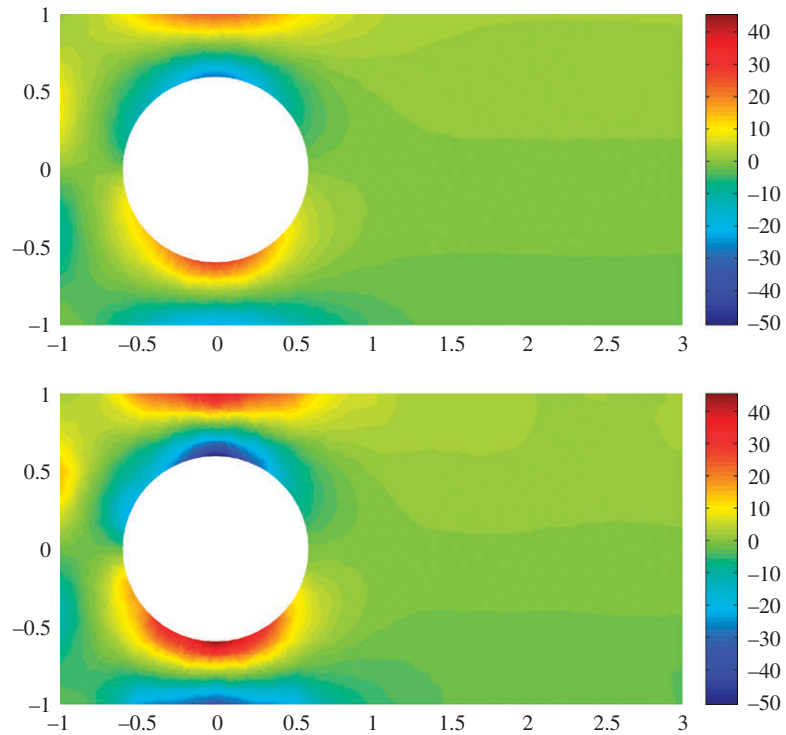


Figure 13. Vorticity plot of the weighted  $L^2$  LSFEM (12) (top) and the SVP formulation (29) (bottom) for the flow past a cylinder  $r=0.6$ .

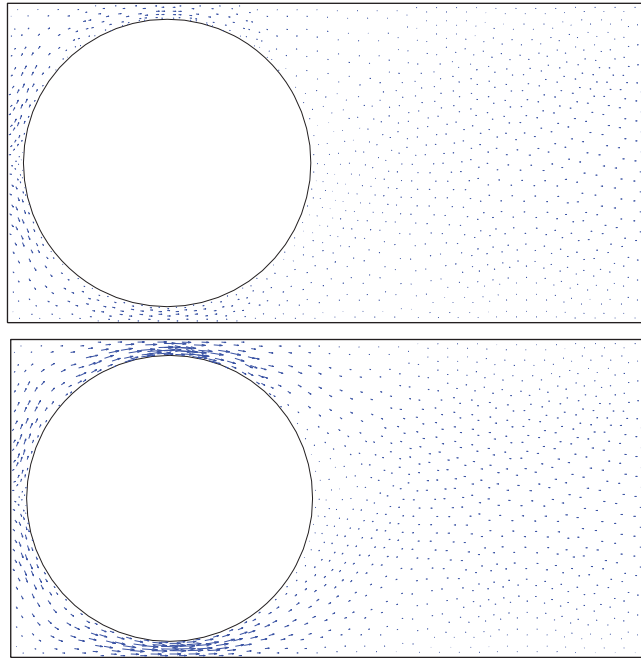


Figure 14. Velocity plot of the weighted  $L^2$  LSFEM (12) (top) and the SVP formulation (29) (bottom) for the flow past a cylinder with  $r=0.9$ .

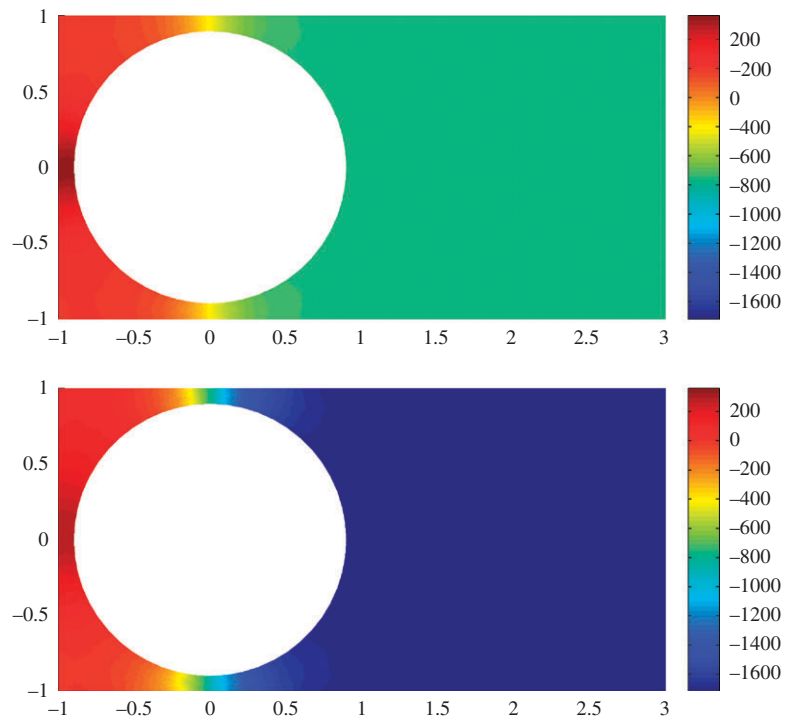


Figure 15. Pressure plot of the weighted  $L^2$  LSFEM (12) (top) and the SVP formulation (29) (bottom) for the flow past a cylinder  $r=0.9$ .

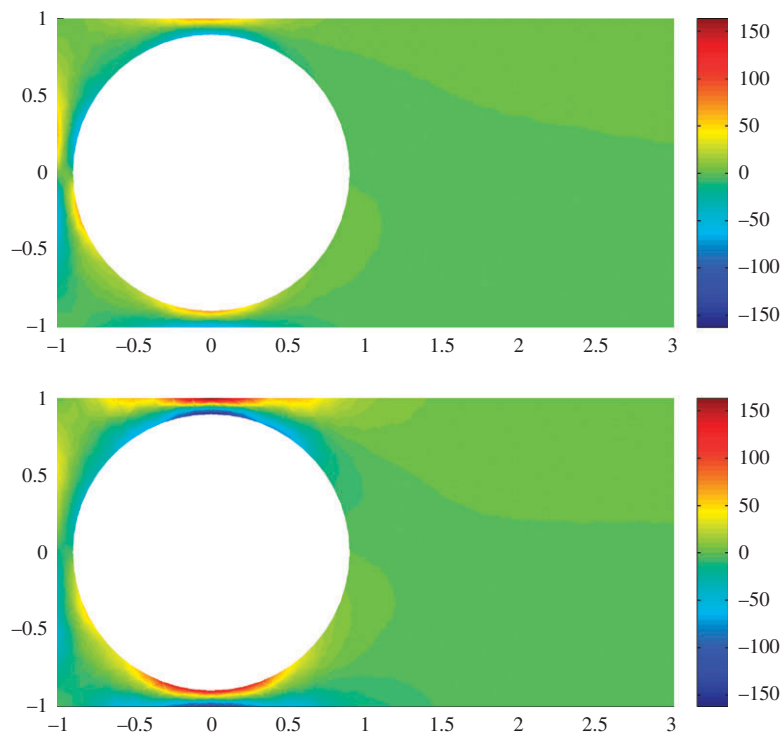


Figure 16. Vorticity plot of the weighted  $L^2$  LSFEM (12) (top) and the SVP formulation (29) (bottom) for the flow past a cylinder  $r=0.9$ .

## 5. CONCLUSION

In this paper we propose, in two stages, a new discontinuous SVP least-squares method for the Stokes equations. The new formulation is viewed as a *discontinuous* velocity least-squares method, based on the VVP Stokes system, using locally divergence-free basis functions, while retaining standard  $C^0$  elements for the remaining variables. As a result, our approach is flexible, applicable to other least-squares methods, and adaptable to three dimensions. In this paper we choose to define the divergence free basis through a stream-function for simplicity; formulations based on other choices, as well as extensions to three dimensions will be considered in a forthcoming paper.

We support our approach through a series of computational studies that highlight the accurate conservation properties of the new SVP least-squares method. Our experiments also reveal that the SVP formulation is robust and performs reliably over a range of varying test problems without problem-dependent tuning. Furthermore, numerical results suggest that the SVP method is not subject to a minimal order condition for the stream-function, which is an additional property of the formulation. Convergence studies show optimal or near optimal convergence rates for all variables.

## APPENDIX A: IMPLEMENTATION

In this section we highlight several aspects of the of a LSFEM implementation based on the discontinuous SVP functional (29), the discontinuous velocity functional (26), and their parent  $C^0$  functional (12). All three methods are implemented using the Intrepid library [35], and the resulting linear systems solved using the Amesos library [36]; both packages are part of the Trilinos Project [34]. Intrepid is a local framework that provides access to basis function definitions for  $H^1(\Omega)$ ,  $H(\Omega, \text{curl})$  and  $H(\Omega, \text{div})$ -conforming finite element spaces in two and three dimensions.

Implementation of the  $C^0$  formulation (12) uses the HGRAD family of basis functions in Intrepid which are designed to assemble global  $H^1$ -conforming finite element spaces.

Implementations of the discontinuous formulations (26) and (29) also use the HGRAD family on each element. However, keeping velocity degrees of freedom independent of each element  $C^0$  does not enforce continuity. Specifically, because  $\mathbf{u}^h = (u_1^h, u_2^h)$  is a vector-valued function, each component has separate degrees of freedom, and in the cases where  $\mathbf{u}^h$  is discontinuous, each element has its own set of degrees of freedom for  $u_1^h$  and  $u_2^h$ .

### A.1. Transformations

Intrepid basis functions are defined on reference elements and must be mapped to physical coordinates by using an appropriate transformation. Selection of the correct transformation is straightforward in three dimensions but a careful definition is required in two dimensions, especially when transforming the curl of scalar to vector fields.

To determine the proper transformation of  $\nabla \times \phi$  (curl of a scalar field in two dimensions) we note that the definition in (2) is also obtained by applying the standard curl operator to the vector field  $(0, 0, \phi(x, y))$ . Therefore,  $\nabla \times \phi$  transforms as an element of  $H(\Omega, \text{div})$ , i.e. by using the Piola transform. Implementation of this transform is available through the HDIVtransformVALUE family of transformations in Intrepid.

The correct transformation of  $\nabla \times \nabla \times \phi$  is obtained by noting that  $\nabla \times \mathbf{v}$ , for a vector-valued function  $\mathbf{v}$ , is the divergence of the *rotated* field  $(v_2, -v_1)$ . Therefore, if  $\nabla \times \phi$  transforms as an  $H(\Omega, \text{div})$  field, it follows that  $\nabla \times \nabla \times \phi$  transforms as the divergence of such a field, i.e. it must be scaled by  $J^{-1}$  where  $J$  is the Jacobian of the reference to physical element map. This transformation is implemented in the HDIVtransformDIV family of methods.

Computation of the curl of a scalar basis function in two dimensions is a standard Intrepid operation which is used to evaluate the reference element values of  $\nabla \times \phi$ . To compute the reference values of  $\nabla \times \nabla \times \phi$  we use the identity

$$\nabla \times \nabla \times \phi = -\phi_{xx} - \phi_{yy}.$$

Thus, on a reference element, we can compute  $\nabla \times \nabla \times \psi$  by using OPERATOR\_D2 which returns all second derivatives of  $\phi$ .

### A.2. Boundary conditions

For our numerical experiments, we use the velocity boundary condition where  $\mathbf{u}|_{\partial\Omega} = \mathbf{u}_\Gamma$ , or  $\psi|_{\partial\Omega} = \psi_\Gamma$  is specified on the entire boundary and set the pressure to 0 at a single point. Since the basis in Intrepid is interpolatory, these boundary conditions are set strongly by specifying, e.g.

$$\begin{aligned} \mathbf{u}(x_i) &= \mathbf{u}_\Gamma(x_i) \quad \forall x_i \in \partial\Omega \\ p(x_0) &= 0 \end{aligned}$$

This is accomplished by defining a vector  $\mathbf{u}_0$  to be zero for all degrees of freedom corresponding to interior points and equal to  $\mathbf{u}_\Gamma$  at the boundary degrees of freedom. We then set

$$\mathbf{b} \leftarrow \mathbf{b} - \mathbf{A}\mathbf{u}_0.$$

Each row and column of  $\mathbf{A}$  corresponding to a boundary degree of freedom is set to zero and the diagonal is set to 1.

### ACKNOWLEDGEMENTS

This work was partially supported by the NSF, grant number DMS 07-46676. The work of James Lai was supported in part by Sandia's Computer Science Research Institute Summer Student Program. We thank Denis Ridzal, Kara Peterson and Chris Siefert for their insight about Trilinos and Intrepid and for their many helpful discussions. Sandia National Laboratories is a multi-program laboratory operated by Sandia Corporation, a wholly owned subsidiary of Lockheed Martin Corporation, for the U.S. Department of Energy's National Nuclear Security Administration under contract DE-AC04-94AL85000.

## REFERENCES

1. Bochev P, Gunzburger M. *Least-squares Finite Element Methods*. Springer: Berlin, 2009.
2. Chang C, Nelson J. Least-squares finite element method for the Stokes problem with zero residual of mass conservation. *SIAM Journal on Numerical Analysis* 1997; **34**:480–489.
3. Bolton P, Thatcher R. On mass conservation in least-squares methods. *Journal of Computational Physics* 2005; **203**:287–304.
4. Deang J, Gunzburger M. Issues related to least-squares finite element methods for the Stokes problem. *SIAM Journal on Numerical Analysis* 1998; **35**:878–906.
5. Heys J, Lee E, Manteuffel T, McCormick S. On mass-conserving least-squares methods. *SIAM Journal on Scientific Computing* 2006; **28**:1675–1693.
6. Heys J, Lee E, Manteuffel T, McCormick S. An alternative least-squares formulation of the Navier–Stokes equations with improved mass conservation. *Journal of Computational Physics* 2008; **226**:994–1006.
7. Heys J, Lee E, Manteuffel T, McCormick S, Ruge J. Enhanced mass conservation in least-squares methods for Navier–Stokes equations. *SIAM Journal on Scientific Computing* 2009; **31**:2303–2321.
8. Kattelans T, Heinrichs W. Conservation of mass and momentum of the least-squares spectral collocation scheme for the stokes problem. *Journal of Computational Physics* 2009; **228**:4649–4664.
9. Proot MM, Gerritsma MI. Mass- and momentum conservation of the least-squares spectral element method for the Stokes problem. *Journal of Scientific Computing* 2006; **27**:389–401.
10. Cai Z, Manteuffel T, McCormick S, Ruge J. First-order system  $\mathcal{L}\mathcal{L}^*$  (FOSLL)\*: scalar elliptic partial differential equations. *SIAM Journal on Numerical Analysis* 2001; **39**:1418–1445.
11. Pontaza J, Reddy J. Space–time coupled spectral/hp least-squares finite element formulations for the incompressible Navier–Stokes equations. *Journal of Computational Physics* 2004; **197**:418–459.
12. Bochev P, Gunzburger M. A locally conservative mimetic least-squares finite element method for the Stokes equations. In *Proceedings of LSSC 2009*, Lirkov I, Margenov S, Wasniewski J (eds). Lecture Notes in Computer Science, vol. 5910. Springer: Berlin: 2009; 637–644.
13. Cai Z, Shin BC. The discrete first-order system least squares: the second-order elliptic boundary value problem. *SIAM Journal on Numerical Analysis* 2002; **40**(1):307–318.
14. Bergström R. Adaptive finite element methods for Div-curl problems. *Ph.D. Thesis*, Chalmers University of Technology, Goteborg, Sweden, 2002.
15. Bergström R, Larson M. Discontinuous least-squares finite element method for the div-curl problem. *Numerische Mathematik* 2005; **101**:601–617. DOI: 10.1007/s00211-005-0600-y.
16. Proot MM, Gerritsma MI. Analysis of a discontinuous least squares spectral element method. *Journal of Scientific Computing* 2002; **17**:297–306.
17. Cao Y, Gunzburger M. Least-squares finite element approximations to solutions of interface problems. *SIAM Journal on Numerical Analysis* 1998; **35**:393–405.
18. Bochev P, Day D. Analysis and computation of a least-squares method for consistent mesh tying. *The Journal of Computational and Applied Mathematics* 2008; **218**:21–33.
19. Bramble J, Pasciak J. Least-squares methods for Stokes equations based on a discrete minus one inner product. *The Journal of Computational and Applied Mathematics* 1996; **74**:155–173.
20. Bochev P, Gunzburger M. Analysis of least-squares finite element methods for the Stokes equations. *Mathematics of Computation* 1994; **63**:479–506.
21. Bochev P, Gunzburger M. Least-squares for the velocity–pressure–stress formulation of the Stokes equations. *Computer Methods in Applied Mechanics and Engineering* 1995; **126**:267–287.
22. Bochev P. Negative norm least-squares methods for the velocity–vorticity–pressure Navier–Stokes equations. *Numerical Methods for PDEs* 1999; **15**:237–256.
23. Raviart PA, Thomas JM. A mixed finite element method for second order elliptic problems. *Mathematical Aspects of the Finite Element Method*, Galligani I, Magenes E (eds). Lecture Notes in Mathematics, vol. 606. Springer: New York, 1977.
24. Austin T, Manteuffel T, McCormick S. A robust approach to minimizing H(div) dominated functionals in an H1-conforming finite element space. *Journal of Numerical Linear Algebra with Applications* 2004; **11**:115–140.
25. Manteuffel T, Ressel K, Starke G. A boundary functional for the least-squares finite element solution of neutron transport problems. *SIAM Journal on Numerical Analysis* 2000; **37**:556–586.
26. Cao Y, Gunzburger M. Least-squares finite element approximations to solutions of interface problems. *SIAM Journal on Numerical Analysis* 1998; **35**:393–405.
27. Bernardi C, Coppoletta G, Girault V, Maday Y. Spectral methods for the Stokes problem in stream-function formulation. *Computer Methods in Applied Mechanics and Engineering* 1990; **80**:229–236.
28. Dubois F, Salaün M, Salmon S. Vorticity–velocity–pressure and stream function–vorticity formulations for the Stokes problem. *Journal de Mathématiques Pures et Appliquées* 2003; **82**:1395–1451.
29. Girault V, Raviart P. *Finite Element Methods for Navier–Stokes Equations*. Springer: Berlin, 1986.
30. Dean E, Glowinski R, Pironneau O. Iterative solution of the stream function–vorticity formulation of the Stokes problem, applications to the numerical simulation of incompressible viscous flow. *Computer Methods in Applied Mechanics and Engineering* 1991; **87**:117–155.
31. Ghia U, Ghia K, Shin C. High-resolutions to incompressible flow using the Navier–Stokes equations and a multigrid method. *Journal of Computational Physics* 1982; **48**:387–411.

32. Cockburn B, Kanschat G, Schötzau D. A locally conservative LDG method for the incompressible Navier–Stokes equations. *Mathematics of Computation* 2004; **74**:1067–1095.
33. Cockburn B, Kanschat G, Schötzau D. A note on discontinuous Galerkin divergence-free solutions of the Navier–Stokes equations. *Journal of Scientific Computing* 2007; **31**:61–73.
34. Heroux M, Bartlett R, Howle V, Hoekstra R, Hu J, Kolda T, Lehoucq R, Long K, Pawlowski R, Phipps E, Salinger A, Thornquist H, Tuminaro R, Willenbring J, Williams A. An Overview of Trilinos. *Technical Report SAND2003-2927*, Sandia National Laboratories, 2003.
35. Bochev P, Ridzal D, Peterson K. *Intrepid: Interoperable Tools for Compatible Discretizations*. <http://trilinos.sandia.gov/packages/intrepid/>, 2010.
36. Sala M, Stanley K, Heroux M. Amesos: a set of general interfaces to sparse direct solver libraries. *Proceedings of PARA'06 Conference*, Umea, Sweden, 2006.